Materials Advances

ROYAL SOCIETY OF CHEMISTRY

PAPER

View Article Online
View Journal

Cite this: DOI: 10.1039/d5ma01423a

Piezoelectrically-enhanced 230 nm far-UV second harmonic generation in a polarity-inversion-free AlN/AlGaN strained-layer superlattice channel waveguide

Shahzeb Malik, *[a] Ryo Momosaki,[a] Hiroto Honda,[a] Kanako Shojiki,[b] Hideto Miyake,[c] Masahiro Uemukai,[ad] Tomoyuki Tanikawa*[ad] and Ryuji Katayama[ad]

Received 6th December 2025, Accepted 30th January 2026

DOI: 10.1039/d5ma01423a

rsc.li/materials-advances

Far-ultraviolet (UV) light has a wide range of global applications, including virus inactivation, bacterial disinfection, human body sterilization, communication, and sensing. Nitride semiconductors, such as AlN and AlGaN, are particularly advantageous for wavelength conversion applications because of their large energy bandgap of approximately 6 eV, which provides excellent transparency in the far-ultraviolet spectrum. In this study, we employed a transverse-quasi-matching approach to design and fabricate an AlN/AlGaN strained-layer superlattice (SLS) channel waveguide. The wavelength spectra and power dependency of the SH intensity confirm the first successful demonstration of far-UV light emission from a polarity-inversion-free SLS structure *via* the enhancement of the second-order nonlinear optical susceptibility by piezoelectric polarization under ultrashort pulse stimulation.

Open Access Article. Published on 30 March 2026. Downloaded on 4/20/2026 5:38:03 AM. This article is licensed under a Creative Commons Attribution 3.0 Unported Licence.

Introduction

AlN- and AlGaN-based far-UV light sources are highly effective for viral inactivation and bacterial disinfection. These ultraviolet (UV) light sources are non-toxic and devoid of dangerous arsenic, mercury and lead. The optimal virus inactivation efficiency of deep-UV light is achieved at a wavelength of 260 nm.[1–4] Low-pressure mercury lamps producing UV light at a wavelength of 254 nm have previously been used in these applications; however, AlGaN-based light-emitting diodes (LEDs) with a wavelength of approximately 260 nm have recently replaced mercury lamps owing to their superior efficiency, environmental sustainability, and long lifespan.[5–7] Nonetheless, these UV light wavelengths are detrimental to human skin as they can obliterate human cells. Conversely, a 230-nm far-UV light source, which has high disinfection and sterilization efficacy, can be utilized in the presence of human skin because the stratum corneum absorbs this wavelength of far-UV light and is non-harmful even with direct exposure to the human body.[8–10] Far-UV germicidal application for air, surfaces, food, and water has been previously reported when mercury (Hg) UV lamps were utilized instead of other far-UV light sources. Recent findings indicate that the COVID-19 pandemic significantly altered the dynamics of the far-UV light industry, particularly accelerating the growth of UV sterilization, purification, and disinfection applications beyond the initial projections made in 2017.[11,12] Excimer lamps emitting at a wavelength of 222 nm are commercially available. However, they are hindered by significant limitations, including high costs attributed to the utilization of expensive gases, large size, low efficiency, and limited lifetime. AlN and AlGaN-based LEDs possess significant potential to supplant excimer lamps because of their reported emission at the shortest wavelength of 210 nm.[13,14] The global far-UV LED market was valued at USD 915.7 million in 2024 and is projected to expand at a compound annual growth rate (CAGR) of 31.6% from 2025 to 2034.[15] However, commercially available far-UV light sources are limited in quantity and are somewhat expensive. It is challenging to further shorten the emission wavelength, and preserving a high wall-plug efficiency is particularly difficult owing to the insulating nature of wide-bandgap materials.[12,16] Owing to the same reason as AlGaN Fabry–Perot laser diodes (LDs), the shortest emission wavelength is 274 nm during continuous-wave operation.[17] The advancement of far-UV LEDs and LDs remains problematic owing to the insulation characteristics of AlGaN, difficulty in impurity doping, and carrier

[a] *Graduate School of Engineering, The University of Osaka, Suita, Osaka 565-0871, Japan. E-mail: malik.s@qoe.eei.eng.osaka-u.ac.jp, tanikawa.tomoyuki.eei.eng@osaka-u.ac.jp*

[b] *Department of Electronic Science and Engineering, Kyoto University, Kyoto 615-8510, Japan*

[c] *Graduate School of Engineering, Mie University, 1577 Kurimamachiya, Tsu, Mie 514-8507, Japan*

[d] *Quantum Information and Quantum Biology Division, Institute for Open and Transdisciplinary Research Initiatives, The University of Osaka, Toyonaka, Osaka 560-0043, Japan*

© 2026 The Author(s). Published by the Royal Society of Chemistry

Open Access Article. Published on 30 March 2026. Downloaded on 4/20/2026 5:38:03 AM.
This article is licensed under a Creative Commons Attribution 3.0 Unported Licence.

injections. Consequently, an innovative method is required for the fabrication and advancement of far-UV light sources.

Presently, far-UV light sources predominantly utilize ArF, KrF, and Ar-ion gases, as well as higher harmonics produced by infrared lasers (Nd: YAG and Ti: sapphire).[18] Wavelength conversion technology is an efficient approach for generating far-UV light. Various bulk crystals, including β-BaB_2O_4 (BBO) and $CsLiB_6O_{10}$ (CLBO), have been extensively utilized for wavelength conversion techniques in industrial applications.[19,20] In these commercially available devices, high conversion efficacy can only be achieved at high-power excitation owing to the minimal nonlinear optical coefficients. Waveguide devices with quasi-phase matching (QPM) structures exhibit a periodic polarity inversion along the longitudinal direction to obtain a high conversion efficiency owing to the extended interaction duration while maintaining a high power density even under low-power excitation levels.[21] The second-harmonic generation (SHG) emission wavelength from devices with ferroelectric materials such as $LiNbO_3$ and $LiTaO_3$ has gradually been shortened toward 300 nm owing to the large nonlinear optical coefficients and availability for fabricating periodic polarity inversion structures by external voltage application.[22,23] However, the far-UV regime is inaccessible because of its limited transparency range. Another intriguing nonlinear optical crystal, $LaBGeO_5$, although transparent at a wavelength of 190 nm, cannot achieve efficient wavelength conversion owing to its small optical nonlinearity.[24]

AlN has recently emerged as an excellent candidate for far-UV light generation *via* SHG because of its substantial second-order nonlinear optical susceptibility along the *c*-axis, which ranges from 4 to 7 pm V^{-1}. Furthermore, AlN exhibits strong thermal conductivity (approximately 370 W mK^{-1}) and a broad transparency range (200 nm to 1.5 μm), leading to a substantial optical damage threshold and broad spectral tunability.[25–29] Modal dispersion phase matching (MDPM),[30–33] coupling-length phase matching (CLPM),[30–33] birefringence phase matching (BPM),[34] and QPM[35,36] have been reported as methods to satisfy phase-matching conditions. Given that birefringence is not achievable in AlN, it appears that SHG of laser light with MDPM, CLPM, and QPM are possible alternative methods.[18] QPM can be accomplished *via* two methods: periodically altering the material polarity along the propagating direction (longitudinal QPM, LQPM) or vertically inverting the polarity across the waveguide (transverse QPM, TQPM). A LQPM device structure based on a waveguide has predominantly been employed for the wavelength conversion process made by electric-field poling for ferroelectric materials, demonstrating high efficiency owing to its access to the materials' largest nonlinear optical susceptibility.[37,38] SHG in AlN waveguides has been proven as an alternative to electrically injected ultraviolet light sources, utilizing third-order LQPM facilitated by polarity-engineered structures, resulting in UV emission at around 344 nm wavelengths,[18] but its conversion efficiency was nearly one order of magnitude lower than that of a first-order LQPM structure. Therefore, the fabrication of first-order LQPM structures for 250–270 nm UV light has also been reported, but SHG has not been reported yet,[43,44] probably because of the difficulty in realizing a high-quality and low-loss short-period polarity-inverted waveguide with smooth sidewalls.

The TQPM enables phase matching through the MDPM between the zeroth-order fundamental mode and higher-order second harmonic (SH) guided modes, while the nonlinear optical interaction is enhanced by inverting the polarity at the nodes of the SH modal distribution.[39–41] UV SHG at a wavelength of 306 nm has been demonstrated in an AlN waveguide with a thickness satisfying the MDPM,[42] but there have been no reports of TQPM attempts from groups other than ours. In a previous study, we proposed and fabricated a novel structure, a TQPM SHG channel waveguide, including a vertically stacked polarity-inverted AlN bilayer.[21] The polarity inversion methods for AlN have been reported elsewhere.[45–47] A channel waveguide comprises an Al-polar/N-polar AlN (+*c*/−*c* AlN) multilayer, fabricated *via* sputtering and subsequent face-to-face annealing (Sp-FFA),[46] successfully demonstrating a 229 nm far-UV SHG.[21] While MDPM, polarity-inverted TQPM, and piezoelectrically enhanced polarity-inversion-free TQPM all demand precise control of the longitudinal phase mismatch, the MDPM results in a low conversion efficiency owing to the lack of efficient nonlinear optical coupling, and polarity-inverted TQPM-based strategies place additional burdens, such as a well-defined epitaxial polarity-inversion method or deliberately wafer bonding technology, both of which complicate the sample fabrication process.[48,49] This endeavor seeks to surmount the barriers and present innovative concepts to enhance the efficacy of far-UV light by adopting a polarization-inversion-free TQPM approach.

In addition to nonlinear optical applications, AlN/AlGaN heterostructures have been thoroughly advanced for deep-ultraviolet optoelectronic devices, such as n^+-AlGaN tunnel-junction concepts proposed for 254 nm DUV LEDs, and recent reviews summarize the progress toward high-efficiency UVB AlGaN LEDs in the 290–310 nm band.[50,51] Research on (0001)-oriented AlN/AlGaN quantum wells and quantum dots has provided complementary insights into the quantum-confined optical properties of closely related nitride.[52]

In this study, we fabricated a polarity-inverted-free Al-polar AlN/AlGaN strained-layer superlattice (SLS) waveguide to introduce a novel method for modulating the effective d_{33} *via* third-order nonlinear optical effects by strong piezoelectric polarization rather than spontaneous polarization inversion, that is, crystallographic polarity inversion. The primary purpose of growing AlN/AlGaN SLSs was to simplify the device fabrication process compared to previously reported device structures for SHG processes and to enhance the nonlinear coupling coefficient by harnessing the piezoelectric field in the TQPM device. TQPM, based on the spatial modulation of the nonlinear optical constants d_{33} and modal dispersion, can increase the wavelength conversion efficiency. As a result, far-UV SHG at 230 nm was successfully demonstrated. This study provides an in-depth analysis of the far-UV SHG device structure, methodology, fabrication processes, and optical results.

 © 2026 The Author(s). Published by the Royal Society of Chemistry

Open Access Article. Published on 30 March 2026. Downloaded on 4/20/2026 5:38:03 AM.
This article is licensed under a Creative Commons Attribution 3.0 Unported Licence.

Methodology

In nonlinear optics, the polarization P of a material in response to a fundamental optical field E^{ω} without static electrical field is described by a power series expansion:

$$P = P^{\omega} + P^{2\omega} + P^{3\omega} + \cdots = \varepsilon_0\chi_{\rm sp}^{(1)}E^{\omega} + \varepsilon_0\chi_{\rm sp}^{(2)}(E^{\omega})^2 + \varepsilon_0\chi_{\rm sp}^{(3)}(E^{\omega})^3 + \cdots, \quad (1)$$

where the i-th term induces nonlinear polarization *via* i-th-order nonlinear optical susceptibility $\chi_{\rm sp}^{(i)}$. When a strong piezoelectric field $E_{\rm pz}$ is applied in the material, third-order nonlinear susceptibility contributes to the second-order nonlinear process as a contribution of nonnegligible four-wave frequency mixing $\chi^{(3)}(-2\omega;\omega,\omega,0)$. The second-order nonlinear polarization $P^{2\omega}$ then becomes

$$P^{2\omega} = \varepsilon_0(\chi_{\rm sp}^{(2)} + \chi^{(3)}E_{\rm pz})(E^{\omega})^2 = \varepsilon_0\chi_{\rm eff}^{(2)}(E^{\omega})^2. \quad (2)$$

Therefore, the effective second-order susceptibility $\chi_{\rm eff}^{(2)}$ is described as

$$\chi_{\rm eff}^{(2)} = \chi_{\rm sp}^{(2)} + \chi^{(3)}E_{\rm pz}. \quad (3)$$

In prior investigations, researchers have employed the second-order nonlinear optical susceptibility to augment the nonlinear optical coefficient $\chi_{\rm eff}^{(2)}$ by using eqn (2). Upon fulfillment of the MDPM condition, the wavelength conversion efficiency is determined by

$$\eta = \tan h^2\left(\kappa\sqrt{P_0}L\right) \quad (4)$$

where L represents the length of the waveguide, P_0 denotes the fundamental wave power, and κ signifies the nonlinear coupling coefficient. κ is directly correlated to the nonlinear optical constant $d_{33}(=\chi_{\rm eff}^{(2)}/2)$ and is expressed as,

$$\kappa = \frac{2\omega\varepsilon_0}{4}\iint[E^{\omega}(x,y)]^2 d_{33}(x,y)E^{2\omega}(x,y){\rm d}x{\rm d}y, \quad (5)$$

where ω is the angular frequency of the fundamental wave, ε_0 is the dielectric constant vacuum. $d_{33}(x,y)$ in eqn (5) represents the situation of TQPM that has spatial modulation. For materials with a wurtzite crystal structure, such as AlN and GaN, the $d_{33}(x,y)$ component isss the dominant coefficient utilized when all interacting fields are polarized along the crystal's c-axis. The overlap integral in eqn (5) represents the strength of the coupling of the square of the fundamental wave $[E^{\omega}(x,y)]^2$ and the SH wave $[E^{2\omega}(x,y)]^2$ *via* $d_{33}(x,y)$. In this study we enhanced the nonlinear coupling coefficient by introducing a novel approach for modulating the d_{33} by utilizing the third-order nonlinear optical effects induced from a strong piezoelectric field $E_{\rm pz}$ in the SHG TQPM device structure instead of polarity inversion. If the introduction of the strain in the SLS considerably increases the piezoelectric field $E_{\rm pz}$ and alters the sign of $d_{33}(x,y)$ from those of AlN layers, the enhancement of κ as shown in Fig. 1(a). On the other hand, we have also investigated the impact of recently reported $\chi_{\rm eff}^{(2)}$ values of multiple quantum wells (MQWs) on sign of $d_{33}(x,y)$. MQWs are based on AlN and AlGaN multiple layers and show an increment of approximately 9.76 times to 20 times more than the previously reported values of $\chi_{\rm eff}^{(2)}$, and κ enhancement can be shown in Fig. 1(a) and (c).[53] The utilization of $\chi_{\rm eff}^{(2)}$ for the SLS structure leads to κ values as shown in Fig. 1(b). The cross-sectional dimension of the channel waveguide was designed to comply with the MDPM requirement between a 460 nm fundamental wave of the first-order TM_{00}-guided mode and a 230 nm SH wave of the second-order TM_{02} mode. The TM-polarized fundamental wave was selected to capitalize on the highest nonlinear optical tensor component d_{33} of AlN, resulting in the generation of a TM-polarized SH wave. The subsequent sections provide a comprehensive explanation of the design and fabrication of the device.

Design of SHG device

A cross-sectional schematic of the TQPM device structure based on a polarity-inversion-free AlN/AlGaN SLS is shown in Fig. 2. The channel waveguide had an ultra-thin AlN layer with a thickness of 84 nm on a sapphire substrate, an SLS region consisting of 13 layers of AlGaN and 14 layers of AlN, followed

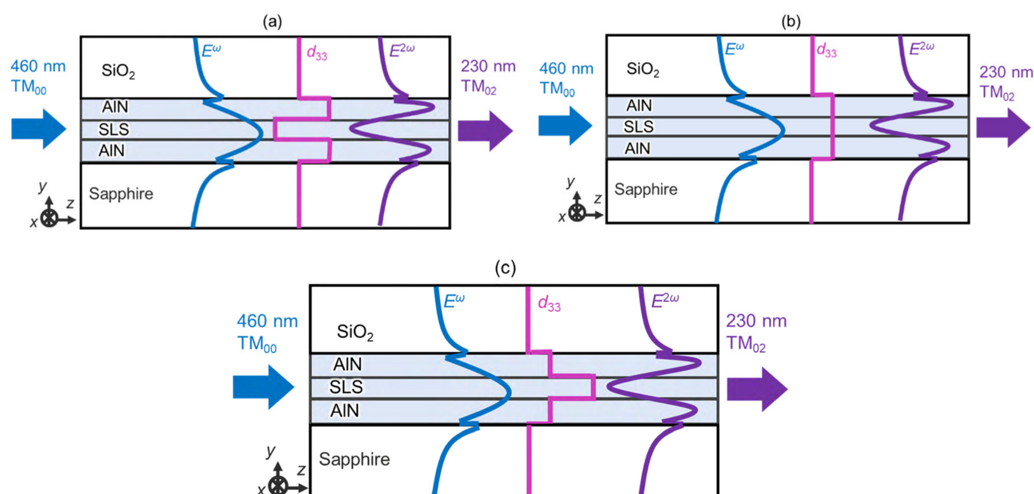

Fig. 1 (a–c) Schematic of a transverse QPM SHG device with a vertical non-polarity-inverted SLS structure.

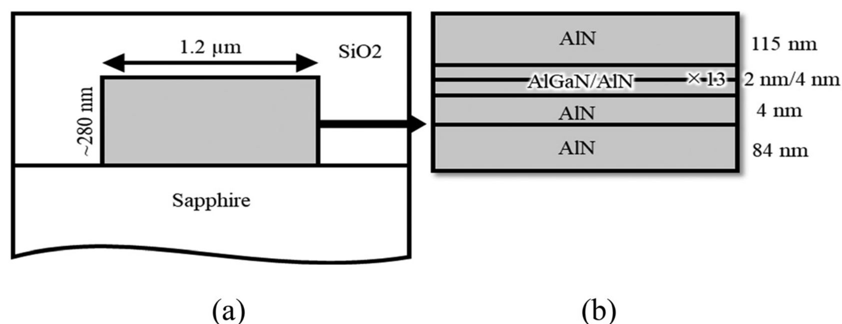

Fig. 2 (a) Cross-sectional TQPM structure of the AlN/AlGaN SLS channel waveguide. (b) Multilayer structure of the channel.

by a 115-nm-thick AlN layer. The thicknesses of the AlGaN and AlN layers were approximately 2 and 4 nm, respectively. The AlN molar fraction in the AlGaN layers was 88%. Silicon dioxide (SiO_2) serves as a cladding layer to protect the channel waveguide during the formation of end facets, despite the reduction in optical confinement.

Using the finite difference method, we solved Maxwell's equations to calculate the effective refractive indices and electric field distributions.[54] Given the utilization of Transverse Magnetic (TM)-polarized waves, the optical constants for AlN, sapphire, and SiO_2 were sourced directly from the published literature, selecting values corresponding to their extraordinary refractive indices. For SLS, an effective medium approach was utilized, assuming that its refractive index was the average of the published AlGaN and AlN refractive indices. The extraordinary refractive indices were used in all calculations. Fig. 3 illustrates the effective refractive indices of the first- and high-order transverse magnetic modes for the fundamental and SH waves, respectively, as a function of waveguide thickness for a channel waveguide width of 1.2 μm. At a channel waveguide thickness of approximately 280 nm, the modal dispersion phase matching (MDPM) condition was satisfied between the TM_{00} guided mode of the fundamental wave at a wavelength of 460 nm and the TM_{02} guided mode of the SH wave at a wavelength of 230 nm. The waveguide thicknesses that satisfied the MDPM conditions between TM_{00} and higher SH modes, specifically TM_{03} and TM_{04}, were estimated to be approximately 432 and 573 nm, respectively. We obtained an average electric field of approximately −0.15 MV cm^{-1} for a fully strained SLS region under no bias voltage application by utilizing SiLENSe 5.14, as shown in Fig. 4(c). The energy band profile shows a reverse-signed piezoelectric contribution across the SLS compared to that of AlN, as shown in Fig. 4(a) and (b). In this study, SiLENSe simulations were performed under the assumption that each AlN/$Al_{0.88}Ga_{0.12}N$ layer remained pseudo-morphically strained to the underlying AlN/sapphire substrate. The SiLENSe simulations assume coherent, fully strained layers with abrupt interfaces, and the resulting electric field represents a spatially averaged polarization field across the SLS region. The strain state and polarization of the SLS structure were calculated theoretically and then compared with the simulation results using SiLENSe 5.14. To compare with the device simulations, we initially employed the conventional III-nitride polarization parameters established by Ambacher and Bernardini,[55,56] which replicate the overall magnitude of the simulated in-plane and out-of-plane strains but show negligible deviation between the contributions of spontaneous and piezoelectric polarizations. Subsequently, we recalculated the polarization using the updated formalism of Dreyer *et al.* and Fichtner *et al.*,[57,58] To confirm the precision of our theoretical framework, we examined the piezoelectric polarization using both the 'proper' and 'improper' constants proposed by Dreyer *et al.* Our analysis showed that improper constants produced significant deviations from the SiLENSe simulation data, leading to polarization values 2.5 times higher than the simulated data. However, the proper constants were very similar to both our simulation results and the values that Bernardini and Ambacher established in the past. The enhancement of κ values without inverting the crystallographic orientation is due to the increment of $\chi^{(2)}_{\text{eff}}$ which was dominated by $\chi^{(3)}E_{\text{pz}}$ term in eqn (2) thanks to the strong average electric field inside the SLS structure,[59,60] where the electric field strength is plotted as a function of position, where the y-axis represents the averaged electric field over the specified spatial domain—in this instance, the full superlattice region spanning from 85 nm to 165 nm above the AlN/sapphire interface. The κ value was obtained by utilizing the $\chi^{(2)}_{\text{eff}}$, $\chi^{(2)}_{\text{MQW}}$ and $\chi^{(3)}$ values from the

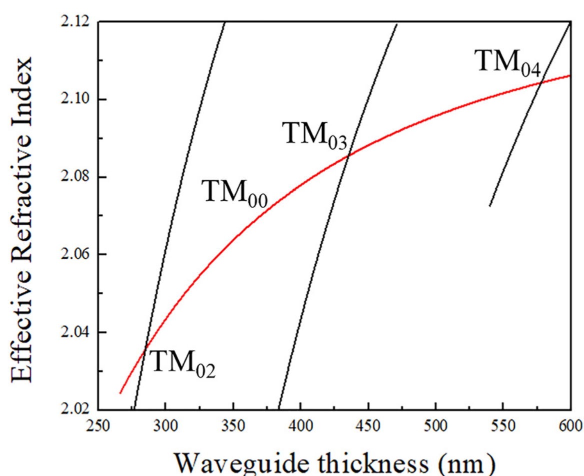

Fig. 3 Effective refractive indices of fundamental (red) and SH (black) modes as a function of waveguide thickness for a 1.2 μm waveguide width.

Open Access Article. Published on 30 March 2026. Downloaded on 4/20/2026 5:38:03 AM.
This article is licensed under a Creative Commons Attribution 3.0 Unported Licence.

© 2026 The Author(s). Published by the Royal Society of Chemistry

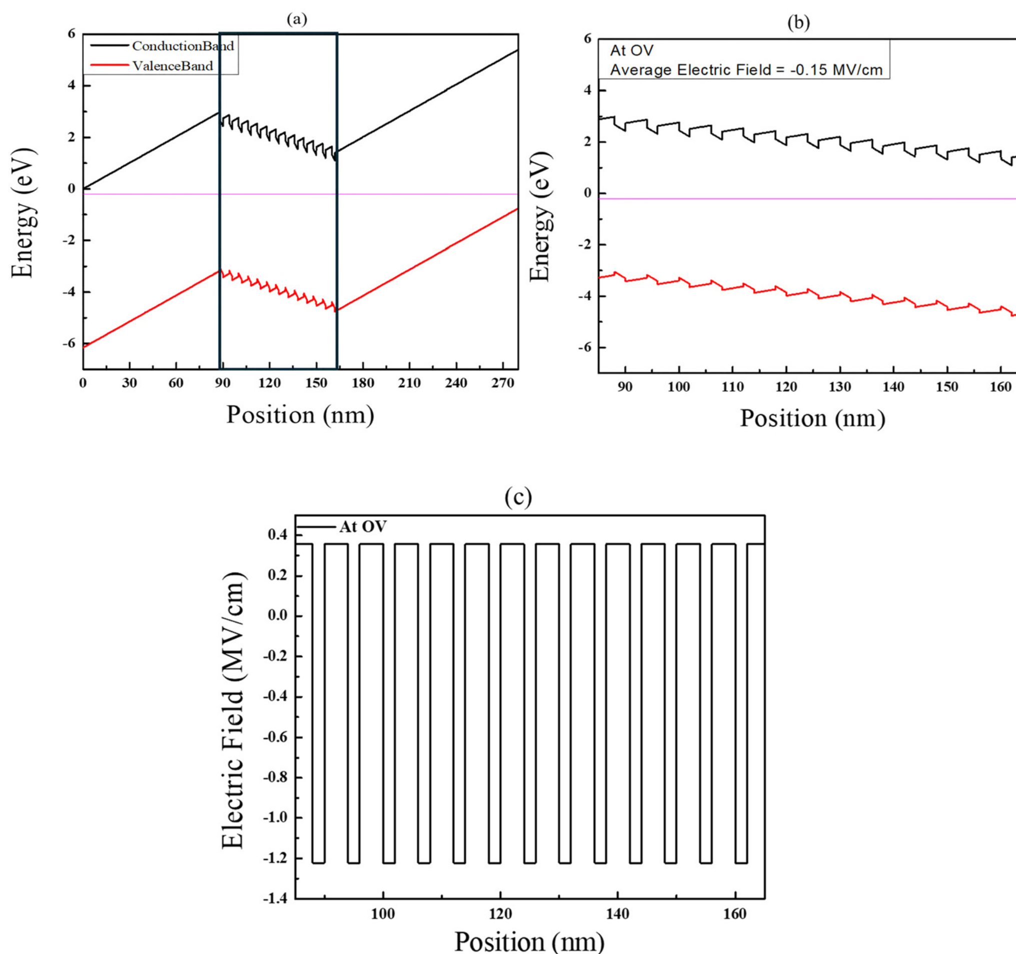

Fig. 4 (a) Energy band profile of the SLS structure. (b) Magnified image of the SLS region, and (c) electric field profile across the SLS region.

Open Access Article. Published on 30 March 2026. Downloaded on 4/20/2026 5:38:03 AM.
This article is licensed under a Creative Commons Attribution 3.0 Unported Licence.

literature: the averaged $\chi^{(2)}_{sp}$ value of 7 pm V^{-1} among several literatures ranging from 1.89 to 3.82 $W^{-1/2}$ cm^{-1} for AlN, and assumed $\chi^{(3)}$ value for GaN of 1.3 × 10^{-20} m^2 V^{-2}.[60,61] For a structure based on AlN/AlGaN MQWs, the reported $\chi^{(2)}_{MQW}$ values are 308.97 pm V^{-1} and −139.7 pm V^{-1}[53] which shows that $\chi^{(3)}$ value might be much larger than the reported $\chi^{(3)}$ value for GaN. Three different pairs of κ values have been calculated based on the $\chi^{(2)}$ values reported in the literature by taking the average electric field of −0.15 MV cm^{-1}. Moreover, we have assumed the $\chi^{(3)}$ value of GaN to find the estimated κ values. The κ values calculated for TM_{02}, TM_{03} and TM_{04} SH modes were 1.23, 0.25 and 0.14 $W^{-1/2}$ cm^{-1}, respectively for considering $\chi^{(2)}_{eff}$ value of AlN in SLS structure. The low value of κ is due to the utilization of extremely small value of $\chi^{(3)}$ for GaN which shows that $\chi^{(3)}E_{pz}$ factor is not enough to alter the sign of d_{33} as shown in Fig. 1(b). Moreover, κ values calculated for TM_{02}, TM_{03} and TM_{04} SH modes were 235.4, 108.8 and 52.76 $W^{-1/2}$ cm^{-1}, respectively for considering $\chi^{(2)}_{MQW}$ value of AlN/AlGaN in SLS structure. These higher κ values are owing to the 20 times enhancement of $\chi^{(2)}_{MQW}$ as compared to $\chi^{(2)}_{sp}$ as shown in Fig. 1(c). Positive $\chi^{(2)}_{MQW}$ might be due to the weaker internal field and the contribution of electric field induced term is small. In addition to this, we have utilized another $\chi^{(2)}_{MQW}$ value of −139.7 pm V^{-1}, this higher negative reported value might be due to the domination of electric field induced term over the intrinsic $\chi^{(2)}$. The calculated κ values for TM_{02}, TM_{03} and TM_{04} SH modes were 112.6, 53.27 and 25.18 $W^{-1/2}$ cm^{-1}, respectively for considering negative $\chi^{(2)}_{MQW}$ value of AlN/AlGaN in SLS structure. These higher values of kappa are due to the alters sign of $d_{33}(x,y)$ as shown in Fig. 1. (a). If we consider the $\chi^{(2)}_{eff}$ value of AlN in SLS structure, the TM_{00}-TM_{02} coupling κ is slightly less than that of the single-layer structure without polarity inversion.[62,63] On the other hand, if we consider the $\chi^{(2)}_{MQW}$ in SLS structure, the TM_{00}–TM_{02} coupling κ is many times higher than that of the single-layer structure without polarity inversion. In one of our previous works, we achieved a κ value of 4.2 $W^{-1/2}$ cm^{-1} with a polarity-inverted AlN bilayer TQPM SHG device.[21] Therefore, in this study, a sufficiently high κ value is expected for experimental demonstration (Table 1).

Fabrication process of SHG device

The fabrication process of the SHG device is shown in Fig. 5. 84-nm-thick ultra-thin AlN layers were fabricated by Sp-FFA on a pair of 2-inch *c*-plane sapphire substrates, as shown in Fig. 5(a). The root-mean-square (RMS) roughness of the AlN layer was 0.13 nm, measured using atomic force microscopy

View Article Online

Table 1 Relationship between $\chi^{(2)}$ (AlN and AlN/AlGaN MQW), effective d_{33}, and the calculated nonlinear coupling coefficient κ (TM_{00}–TM_{02}), taking $\langle E\rangle$ = −0.15 MV cm^{-1}

	d_{33} (pm V^{-1})	$\chi^{(2)}_{eff}$ (pm V^{-1})	$\chi^{(3)}$ (m^2 V^{-2})	κ ($W^{-1/2}$ cm^{-1})
$\chi^{(2)}_{sp}$	7	14	1.3×10^{-20} (GaN)	1.23
$\chi^{(2)}_{MQW}$	308.9	617.7	1.3×10^{-20} (GaN)	235.4
$\chi^{(2)}_{MQW}$	−139.8	−279.6	1.3×10^{-20} (GaN)	112.6

(AFM) in a 5 × 5 μm^2 area. Subsequently, an AlN/$Al_{0.88}Ga_{0.12}N$ SLS structure was fabricated by metalorganic vapor phase epitaxy (MOVPE) over the Sp-FFA AlN layer, as shown in Fig. 5(b). The SLS contains 13 pairs of AlN and $Al_{0.88}Ga_{0.12}N$ layers over the first 4-nm-thin AlN layer. The thicknesses of AlN and $Al_{0.88}Ga_{0.12}N$ in the SLS were 4 and 2 nm, respectively. The thickness of the second AlN guiding layer was 115 nm approximately. The detailed method for the epitaxial growth of SLS has been described elsewhere.[64] After MOVPE growth, the RMS surface roughness was determined to be 0.15 nm. The total thickness of the SLS structure was approximately 280 nm. Fig. 5(c) illustrates the deposition of SiO_2 mask with a thickness of 200 nm onto the SLS structure using radio frequency (RF) sputtering. A negative electron beam (EB) resist was used to create a stripe channel pattern using EB lithography. Subsequently, the stripe pattern was transferred to SiO_2 masks using capacitively coupled plasma reactive ion etching (CCP-RIE) with a CF_4/H_2 gas combination. Inductively coupled plasma RIE (ICP-RIE) using BCl_3 and Cl_2 was performed with an antenna power of 50 W and a bias power of 400 W to fabricate the channel waveguides, as shown in Fig. 5(d). Finally, the end facets of the channel waveguides were formed by dicing and polishing with diamond slurry, as shown in Fig. 5(e). Fig. 5(f) shows a cross-sectional scanning electron microscopic (SEM) image of the TQPM channel waveguide after polishing. The channel waveguide resembled a trapezoid, with sidewalls that were not perpendicular, resulting in a minor impact on the phase matching wavelength and κ.[21] The trapezoidal ridge

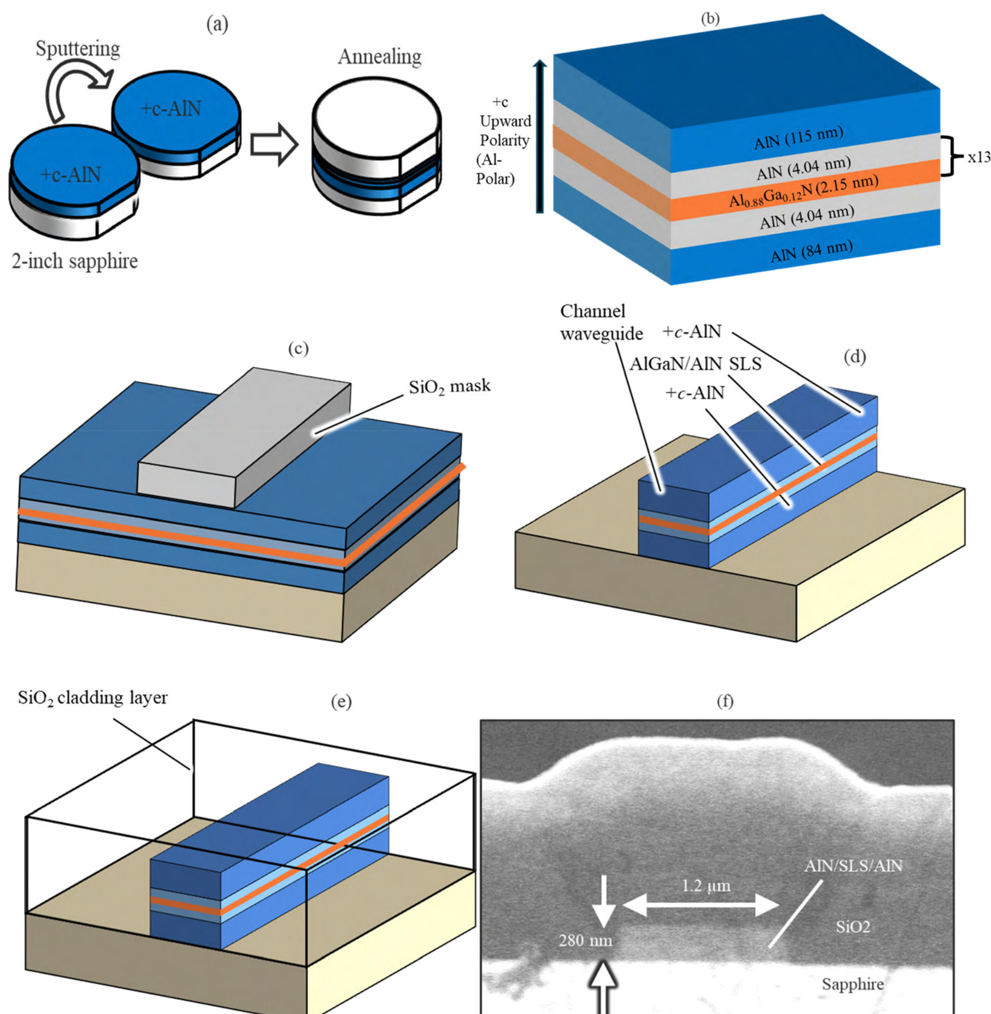

Fig. 5 Fabrication process of TQPM AlN/AlGaN SLS channel waveguide structure. (a) Sputtering and face-to-face annealing of AlN. (b) MOVPE of AlN/AlGaN SLS structure. (c) Formation of SiO_2 mask. (d) Formation of a channel waveguide by ICP-RIE. (e) Deposition of SiO_2 cladding layer, dicing, and end-face polishing. (f) Cross-sectional scanning electron microscopic (SEM) image of the fabricated waveguide.

Open Access Article. Published on 30 March 2026. Downloaded on 4/20/2026 5:38:03 AM.
This article is licensed under a Creative Commons Attribution 3.0 Unported Licence.

© 2026 The Author(s). Published by the Royal Society of Chemistry

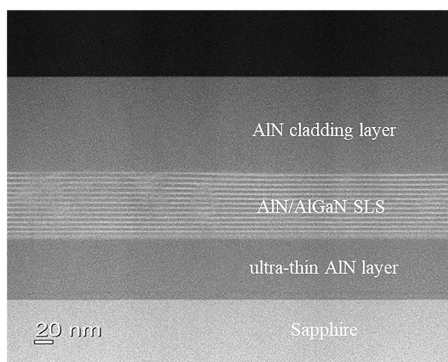

Fig. 6 HAADF-STEM image of the fabricated waveguide device.

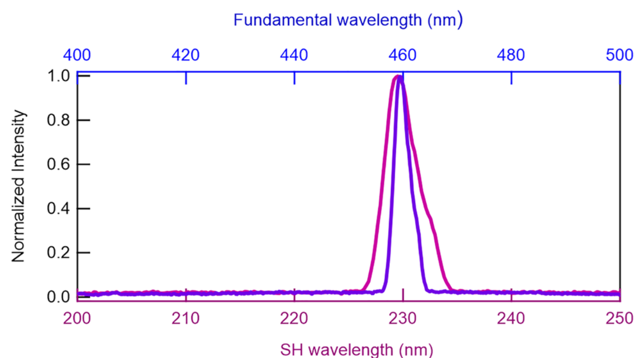

Fig. 7 Wavelength spectra of the pump (blue color) and SH (purple color) waves.

waveguide is expected to alter the computed κ owing to variations in the modal confinement and overlap; however, the qualitative TQPM mechanism, primarily determined by the TM_{02} vertical field configuration and SLS-localized nonlinearity, remains unaltered. The length of the fabricated waveguide was 3 mm.

In addition, the high-angle annular dark-field (HAADF) scanning transmission electron microscopy (STEM) image provides a cross-sectional view of the AlN/AlGaN SLS structure. Consequently, the AlGaN layers were clearly visible as bright stripes sandwiched between the two AlN layers, confirming the successful growth of the entire structure. The abruptness of the interfaces between the layers is evident, indicating a high structural quality (Fig. 6).

Results and discussion

Optical experiments were conducted using a tunable frequency-doubled femtosecond Ti: sapphire laser as the pump source. The polarization and the intensity of the fundamental wave were controlled by using a half-wave plate and a Glan-Thompson prism. The fundamental laser light was concentrated on the channel waveguide using a 100× objective lens to be coupled to the TM polarized mode. The incident angle of the pump light and device angle were adjusted accordingly to achieve the maximum intensity of the fundamental output light which was coupled into a UV optical fiber connected to the charged-coupled device (CCD) spectrometer by a Cassegrain objective lens and an off-axis parabolic mirror. A bandpass filter exhibiting transmittances of 40% at 230 nm and 0.02% at 460 nm was incorporated between the Cassegrain objective lens and the off-axis parabolic reflector. The wavelength of the pump light was set to 460 nm, and we measured the average powers of 1.63, 3.32, 4.54 and 6.03 mW after the 100× objective lens and before the chip. With the spot diameter of approximately 1 μm and pulse width of 100 fs along with the repetition frequency of 80 MHz, the on-chip intensity would be approximately in between 12 to 45 GW cm^{-2} by assuming that all power is coupled into the guided mode.

Fig. 7 shows the spectra of the fundamental and SH light. At a fundamental wavelength of 460 nm, a far-UV SH light emission with a central wavelength of 230 nm has been observed. The full widths at half maximum (FWHMs) for the fundamental and SH spectra were 3.53 and 3.58 nm, respectively. The reason for the wide spectral bandwidth of SH light is the limited effective interaction length due to the group velocity walk-off between the pulses of fundamental and SH waves for ultrashort pulse excitation.[65] The normalized conversion efficiency η_{SH} was not estimated experimentally here but it is roughly estimated to be 10^{-4}% W^{-1}, 5.07% W^{-1} and 22.17% W^{-1} for assuming a d_{33} values of 7 pmV^{-1}, 139 pmV^{-1} and 308.9 pmV^{-1} respectively. These values have been estimated by neglecting propagation and coupling losses. As reported previously in case of blue SHGs from GaN TQPM channel waveguides with ultrashort pulse excitation that due to the short effective interaction of about 20 μm, caused by the severe walk-off, the estimated group velocity mismatch (GVM) is about 10 ps mm^{-1}.

The input power dependence shows that the SH light was directly proportional to the square of the pump light power as shown by a solid line in Fig. 8. Therefore, the far-UV SHG light in a vertical non-inverted AlN/SLS/AlN structure has been confirmed.

Last but not the least, we presented a comprehensive approach to designing and realizing a TQPM-based channel

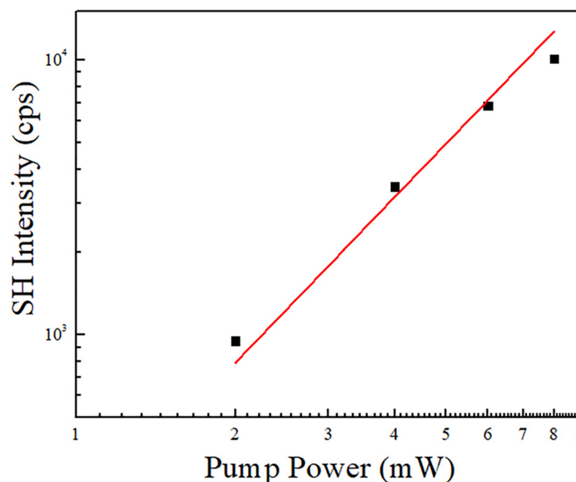

Fig. 8 Dependence of SH intensity on input power.

Open Access Article. Published on 30 March 2026. Downloaded on 4/20/2026 5:38:03 AM.
This article is licensed under a Creative Commons Attribution 3.0 Unported Licence.

waveguide structure aimed at efficient nonlinear optical conversion. The coupling coefficient κ was extracted by leveraging the piezoelectric field distributions simulated using SiLENSe software, supporting the theoretical basis for polarity-inversion-free TQPM. The functionality of the fabricated device has been validated, and we conducted an optical SHG experiment, demonstrating, for the first time, SHG in a SLS structure. This integrated workflow—from simulation to fabrication and optical validation—highlights a scalable path toward high-efficiency SHG devices based on fully-epitaxial-engineered AlN/AlGaN heterostructures.

Conclusion

In conclusion, we introduced a novel method for modulating the d_{33} and third-order nonlinear optical effects by strong piezoelectric polarization in the AlN/AlGaN SLS instead of the polarity inversion. As a result, a QPM channel waveguide has been designed and fabricated by utilizing a polarity-inversion-free structure, and 230 nm far-UV SHG has been confirmed under ultrashort pulse laser excitation. These results demonstrate that the structure is a good candidate for high-efficiency, compact, and cost-effective far-UV light sources. To have a comprehensive understanding, further optical characterization is required, specifically wavelength tolerance and SHG efficiency.

Conflicts of interest

There are no conflicts to declare.

Data availability

All data supporting the findings of this study are available within the article.

References

1 H. Shimoda, J. Matsuda, T. Iwasaki and D. Hayasaka, *J. Photochem. Photobiol.*, 2021, **7**, 100050.
2 T. Minamikawa, T. Koma, A. Suzuki, T. Mizuno, K. Nagamatsu, H. Arimochi, K. Tsuchiya, K. Matsuoka, T. Yasui, K. Yasutomo and M. Nomaguchi, *Sci. Rep.*, 2021, **11**, 1.
3 T. Nambu, T. Yano, S. Umeda, N. Yokoyama, H. Honda, Y. Tanaka, Y. Maegaki, Y. Mori, M. Yoshimura, S. Kobayashi, S. Ichikawa, Y. Fujiwara, R. Ishii, Y. Kawakami, M. Uemukai, T. Tanikawa and R. Katayama, *Opt. Express*, 2022, **30**, 18628.
4 M. Usman, S. Malik and M. Munsif, *Luminescence*, 2020, **35**, 1442.
5 N. Maeda and H. Hirayama, *Phys. Status Solidi C*, 2013, **10**, 1521.
6 A. Pandey, W. J. Shin, J. Gim, R. Hovden and Z. Mi, *Photon. Res.*, 2020, **8**, 331.
7 H. Hirayama, N. Maeda, S. Fujikawa, S. Toyoda and N. Kamata, *Jpn. J. Appl. Phys.*, 2014, **53**, 100209.
8 S. Kreusch, S. Schwedler, B. A. Tautkus, G. A. Cumme and A. Horn, *Anal. Biochem.*, 2003, **313**, 208.
9 M. Buonanno, B. Ponnaiya, D. Welch, M. Stanislauskas, G. Randers-Pehrson, L. Smilenov, F. D. Lowy, D. M. Owens and D. J. Brenner, *Radiat. Res.*, 2017, **187**, 493.
10 K. Narita, K. Asano, Y. Morimoto, T. Igarashi and A. Nakane, *PLoS One*, 2018, **13**, e0201259.
11 Yole Développement, UV LEDs – Market and Technology Trends 2020, Market & Technology Report, October 2020.
12 S. Malik, M. Usman, M. A. Khan and H. Hirayama, *J. Mater. Chem. C*, 2021, **9**, 16545.
13 H. Kitagawa, Y. Kaiki, K. Tadera, T. Nomura, K. Omori, N. Shigemoto, S. Takahashi and H. Ohge, *Photodiagn. Photodyn. Ther.*, 2021, **34**, 102334.
14 Y. Taniyasu, M. Kasu and T. Makimoto, *Nature*, 2006, **441**, 325.
15 https://www.gminsights.com/industry-analysis/uv-c-led-market.
16 N. Lobo-Ploch, F. Mehnke, L. Sulmoni, H. K. Cho, M. Guttmann, J. Glaab, K. Hilbrich, T. Wernicke, S. Einfeldt and M. Kneissl, *Appl. Phys. Lett.*, 2020, **117**, 111102.
17 Z. Zhang, M. Kushimoto, A. Yoshikawa, K. Aoto, C. Sasaoka, L. J. Schowalter and H. Amano, *Appl. Phys. Lett.*, 2022, **121**, 221102.
18 D. Alden, T. Troha, R. Kirste, S. Mita, Q. Guo, A. Hoffmann, M. Zgonik, R. Collazo and Z. Sitar, *Appl. Phys. Lett.*, 2019, **114**, 103504.
19 T. Sasaki, Y. Mori and M. Yoshimura, *Opt. Mater.*, 2003, **23**, 343.
20 J. Sakuma, Y. Asakawa, T. Sumiyoshi and H. Sekita, *IEEE J. Sel. Top. Quantum Electron.*, 2004, **10**, 1244.
21 H. Honda, S. Umeda, K. Shojiki, H. Miyake, S. Ichikawa, J. Tatebayashi, Y. Fujiwara, K. Serita, H. Murakami, M. Tonouchi, M. Uemukai, T. Tanikawa and R. Katayama, *Appl. Phys. Express*, 2023, **16**, 062006.
22 C. Gray, J. R. C. Woods, L. G. Carpenter, H. Kahle, S. A. Berry, A. C. Tropper, M. Guina, V. Apostolopoulos, P. G. R. Smith and C. B. E. Gawith, *Appl. Opt.*, 2020, **59**, 4921.
23 R. T. White, I. T. McKinnie, S. D. Butterworth, G. W. Baxter, D. M. Warrington, P. G. R. Smith, G. W. Ross and D. C. Hanna, *Appl. Phys. B*, 2003, **77**, 547.
24 M. Yamada, N. Nada, M. Saitoh and K. Watanabe, *Appl. Phys. Lett.*, 1993, **62**, 435.
25 Y. Fujii, S. Yoshida, S. Misawa, S. Maekawa and T. Sakudo, *Appl. Phys. Lett.*, 1977, **31**, 815.
26 G. A. Slack, R. A. Tanzilli, R. O. Pohl and J. W. Vandersande, *J. Phys. Chem. Solids*, 1987, **48**, 641.
27 R. Rounds, B. Sarkar, A. Klump, C. Hartmann, T. Nagashima, R. Kirste, A. Franke, M. Bickermann, Y. Kumagai, Z. Sitar and R. Collazo, *Appl. Phys. Express*, 2018, **11**, 071001.
28 M. M. Fejer, G. A. Magel, D. H. Jundt and R. L. Byer, *IEEE J. Quantum Electron.*, 1992, **28**, 2631.
29 S. Sinha, D. S. Hum, K. E. Urbanek, Y.-W. Lee, M. J. F. Digonnet, M. M. Fejer and R. L. Byer, *J. Lightwave Technol.*, 2008, **26**, 3866.
30 T. Sugita, K. Mizuuchi, Y. Kitaoka and K. Yamamoto, *Opt. Lett.*, 1999, **24**, 1590.
31 D. B. Anderson and J. T. Boyd, *Appl. Phys. Lett.*, 1971, **19**, 266.

Open Access Article. Published on 30 March 2026. Downloaded on 4/20/2026 5:38:03 AM.
This article is licensed under a Creative Commons Attribution 3.0 Unported Licence.

© 2026 The Author(s). Published by the Royal Society of Chemistry

Open Access Article. Published on 30 March 2026. Downloaded on 4/20/2026 5:38:03 AM.
This article is licensed under a Creative Commons Attribution 3.0 Unported Licence.

32 P. K. Tien, *Appl. Opt.*, 1971, **10**, 2395.
33 Y. L. Lee, W. Shin, B.-A. Yu, C. Jung, Y.-C. Noh and D.-K. Ko, *Opt. Express*, 2010, **18**, 7678.
34 S. V. Rao, K. Moutzouris and M. Ebrahimzadeh, *J. Opt. A: Pure Appl. Opt.*, 2004, **6**, 569.
35 I. Biaggio, V. Coda and G. Montemezzani, *Phys. Rev. A: At., Mol., Opt. Phys.*, 2014, **90**, 043816.
36 D. Duchesne, K. A. Rutkowska, M. Volatier, F. Legare, S. Delprat, M. Chaker, D. Modotto, A. Locatelli, C. De Angelis, M. Sorel, D. N. Christodoulides, G. Salamo, R. Arès, V. Aimez and R. Morandotti, *Opt. Express*, 2011, **19**, 12408.
37 A. Chowdhury, H. M. Ng, M. Bhardwaj and N. G. Weimann, *Appl. Phys. Lett.*, 2003, **83**, 1077.
38 K. Matsuhisa, H. Ishihara, M. Sugiura, Y. Kawata, A. Sugita, Y. Inoue and T. Nakano, *Funct. Mater. Lett.*, 2021, **14**, 2150034.
39 M. Jager, G. I. Stegeman, M. C. Flipse, M. Diemeer and G. Mohlmann, *Appl. Phys. Lett.*, 1996, **69**, 4139.
40 W. Wirges, S. Yilmaz, W. Brinker, S. Bauer-Gogonea, S. Bauer, M. Jager, G. I. Stegeman, M. Ahlheim, M. Stähelin, B. Zysset, F. Lehr, M. Diemeer and M. C. Flipse, *Appl. Phys. Lett.*, 1997, **70**, 3347.
41 L. Wang, X. Zhang and F. Chen, *Laser Photonics Rev.*, 2021, **15**, 2100409.
42 T. Troha, M. Rigler, D. Alden, I. Bryan, W. Guo, R. Kirste, S. Mita, M. D. Gerhold, R. Collazo, Z. Sitar and M. Zgonik, *Opt. Mater. Express*, 2016, **6**, 2014.
43 J. Wright, C. Moe, A. V. Sampath, G. A. Garrett and M. Wraback, *Phys. Status Solidi C*, 2011, **8**, 2331.
44 D. Alden, W. Guo, R. Kirste, F. Kaess, I. Bryan, T. Troha, A. Bagal, P. Reddy, L. H. Hernandez-Balderrama, A. Franke, S. Mita, C.-H. Chang, A. Hoffmann, M. Zgonik, R. Collazo and Z. Sitar, *Appl. Phys. Lett.*, 2016, **108**, 261106.
45 N. Stolyarchuk, T. Markurt, A. Courville, K. March, J. Zúñiga-Pérez, P. Vennéguès and M. Albrecht, *Sci. Rep.*, 2018, **8**, 14111.
46 K. Shojiki, K. Uesugi, S. Kuboya and H. Miyake, *J. Cryst. Growth*, 2021, **574**, 126309.
47 Z. Liu, Y. Guo, J. Yan, Y. Zeng, J. Wang and J. Li, *Appl. Phys. Express*, 2021, **14**, 085501.
48 L. Wang, X. Zhang and F. Chen, *Laser Photonics Rev.*, 2021, **15**, 2100409.
49 H. Ito and H. Inaba, *Opt. Lett.*, 1978, **2**, 139.
50 M. N. Sharif, M. A. Khan, Q. Wali, P. Zhang, F. Wang and Y. Liu, *Appl. Opt.*, 2022, **61**, 9186.
51 M. A. Khan, Y. Yamada and H. Hirayama, *Phys. Status Solidi A*, 2024, **221**, 2300581.
52 A. Ibanez, N. Nikitskiy, A. Zaiter, P. Valvin, W. Desrat, T. Cohen, M. A. Khan, G. Cassabois, H. Hirayama, P. Genevet, J. Brault and B. Gil, *J. Appl. Phys.*, 2023, **134**, 193103.
53 W. J. Shin, P. Wang, Y. Sun, S. Paul, J. Liu, M. Kira, M. Soltani and Z. Mi, *ACS Photonics*, 2023, **10**, 34.
54 A. B. Fallahkhair, K. S. Li and T. E. Murphy, *J. Light Technol.*, 2008, **26**, 1423.
55 O. Ambacher, J. Smart, J. R. Shealy, N. G. Weimann, K. Chu, M. Murphy, W. J. Schaff, L. F. Eastman, R. Dimitrov, L. Wittmer and M. Stutzmann, *J. Appl. Phys.*, 1999, **85**, 3222.
56 O. Ambacher, O. Ambacher, B. Foutz, J. Smart, J. R. Shealy, N. G. Weimann, K. Chu, M. Murphy, A. J. Sierakowski, W. J. Schaff, L. F. Eastman and R. Dimitrov, *J. Appl. Phys.*, 2000, **87**, 334.
57 C. E. Dreyer, A. Janotti, C. G. Van de Walle and D. Vanderbilt, *Phys. Rev. X*, 2016, **6**, 021038.
58 S. Fichtner, M. Yassine, C. G. Van de Walle and O. Ambacher, *Appl. Phys. Lett.*, 2024, **125**, 040501.
59 Q. Guo, R. Kirste, S. Mita, J. Tweedie, P. Reddy, S. Washiyama, M. H. Breckenridge, R. Collazo and Z. Sitar, *Jpn. J. Appl. Phys.*, 2019, **58**, 050901.
60 X. Liu, A. W. Bruch and H. X. Tang, *Adv. Opt. Photon.*, 2023, **15**, 236.
61 A. Petris, P. Gheorghe, T. Braniste and I. Tiginyanu, *Materials*, 2021, **14**, 3194.
62 J. Miragliotta, D. K. Wickenden, T. J. Kistenmacher and W. A. Bryden, *J. Opt. Soc. Am. B*, 1993, **10**, 1447.
63 N. A. Sanford, A. V. Davydov, D. V. Tsvetkov, A. V. Dmitriev, S. Keller, U. K. Mishra, S. P. Den Baars, S. S. Park, J. Y. Han and R. J. Molnar, *J. Appl. Phys.*, 2005, **97**, 053512.
64 S. Malik, M. Ito, H. Honda, R. Noro, K. Shojiki, H. Miyake, M. Uemukai, T. Tanikawa and R. Katayama, *Cryst. Growth Des.*, 2025, **25**, 3266.
65 Y. Yokoyama, Y. Morioka, T. Murata, H. Honda, K. Serita, H. Murakami, M. Tonouchi, S. Tokita, S. Ichikawa, Y. Fujiwara, T. Hikosaka, M. Uemukai, T. Tanikawa and R. Katayama, *Appl. Phys. Express*, 2022, **15**, 112002.

© 2026 The Author(s). Published by the Royal Society of Chemistry